Theory of Phonon-Mediated Superconductivity in Twisted Bilayer Graphene

Fengcheng Wu, A. H. MacDonald, and Ivar Martin

Phys. Rev. Lett. **121**, 257001 — Published 17 December 2018

DOI: 10.1103/PhysRevLett.121.257001

Theory of Phonon-Mediated Superconductivity in Twisted Bilayer Graphene

Fengcheng Wu,[1,2] A. H. MacDonald,[3] and Ivar Martin[1]

[1] *Materials Science Division, Argonne National Laboratory, Argonne, Illinois 60439, USA*
[2] *Condensed Matter Theory Center and Joint Quantum Institute, Department of Physics, University of Maryland, College Park, Maryland 20742, USA*
[3] *Department of Physics, University of Texas at Austin, Austin, Texas 78712, USA*

We present a theory of phonon-mediated superconductivity in near magic angle twisted bilayer graphene. Using a microscopic model for phonon coupling to moiré band electrons, we find that phonons generate attractive interactions in both s and d wave pairing channels and that the attraction is strong enough to explain the experimental superconducting transition temperatures. Before including Coulomb repulsion, the s-wave channel is more favorable; however, on-site Coulomb repulsion can suppress s-wave pairing relative to d-wave. The pair amplitude varies spatially with the moiré period, and is identical in the two layers in the s-wave channel but phase shifted by π in the d-wave channel. We discuss experiments that can distinguish the two pairing states.

Introduction.— Long-period moiré superlattices form whenever two-dimensional crystals are overlaid with a small difference in lattice constant or orientation, and have recently been employed to alter the electronic [1–6] and excitonic [7–9] properties of two-dimensional materials. One particularly exciting development is the discovery of interaction-induced insulating states accompanied by nearby lobes of superconductivity in twisted bilayer graphene [10, 11]. Both states occur only when the twist angle between layers is close to the largest magic angle [12] at which the low-energy moiré bands [12–15] are nearly flat. The superconducting pairing mechanism of twisted bilayer graphene has not yet been established, and a variety of possibilities are currently being explored [16–29], including routes towards electron-electron interaction mediated superconductivity, and also a phenomenological mean-field theory [23] for s-wave pairing. In this Letter we present a microscopic theory of magic angle superconductivity in twisted bilayer graphene in which the attractive interaction is mediated by the phonon modes of the individual two-dimensional graphene sheets. We find that phonons generate attraction in both s and d wave channels. In combination with the greatly enhanced density-of-states of the flat bands, the attraction in both channels is strong enough to account for the superconducting transition temperatures observed experimentally. The competition between s and d wave channels depends on Coulomb repulsive interaction. We discuss experimental signatures that could be used to distinguish these two pairing states.

Moiré bands.— At small twist angles the single-particle physics of twisted bilayer graphene can be described using a continuum moiré Hamiltonian, in which the atomic-scale commensurability plays no role. To construct the twisted bilayer, we start from AA stacked bilayer graphene, and then rotate the bottom and top layers by angles $-\theta/2$ and $+\theta/2$ around one of the hexagonal plaquette centers. We choose the origin of coordinates to be on this rotation axis and half-way between layers. With respect to this origin, the point group symmetry is D_6, which is generated by a sixfold rotation $\hat{C}_6$ around the $\hat{z}$ axis, and twofold rotations $\hat{\mathcal{M}}_x$ and $\hat{\mathcal{M}}_y$ respectively around the $\hat{x}$ and $\hat{y}$ axes. The operations $\hat{\mathcal{M}}_{x,y}$ swap the two layers. Because spin-orbit interactions are negligible in graphene [30, 31], electrons also have accurate spin SU(2) symmetry and spinless time-reversal symmetry $\hat{\mathcal{T}}$.

At small twist angles the bilayer moiré pattern, illustrated in Fig. 1(a), is anchored by a triangular lattice of regions with local AA inter-layer coordination that has lattice constant $a_M = a_0/[2\sin(\theta/2)]$, where a_0 is the lattice constant of monolayer graphene. Local AB and BA coordination then occur at the corners of the moiré Wigner-Seitz cell. Our theory of phonon-mediated pairing is based on the continuum moiré Hamiltonian for low-energy electrons [12], which is spin-independent and is given in valley $+K$ by:

$$\mathcal{H}_+ = \begin{pmatrix} h_{\mathfrak{b}}(\boldsymbol{k}) & T(\boldsymbol{r}) \\ T^\dagger(\boldsymbol{r}) & h_{\mathfrak{t}}(\boldsymbol{k}) \end{pmatrix}. \tag{1}$$

Here $h_{\mathfrak{b},\mathfrak{t}}$ are the isolated Dirac Hamiltonians of the twisted bottom ($\mathfrak{b}$) and top ($\mathfrak{t}$) layers:

$$h_\ell(\boldsymbol{k}) = e^{-i\ell\frac{\theta}{4}\sigma_z}[\hbar v_F(\boldsymbol{k}-\boldsymbol{\kappa}_\ell)\cdot\boldsymbol{\sigma}]e^{+i\ell\frac{\theta}{4}\sigma_z}, \tag{2}$$

where ℓ is $+1$ (-1) for the $\mathfrak{b}$ ($\mathfrak{t}$) layer, v_F is the bare Dirac velocity($\sim 10^6$ m/s), and $\boldsymbol{\sigma}$ are Pauli matrices that act in the sublattice space. Because of the rotation, the Dirac cone position in layer ℓ is shifted to $\boldsymbol{\kappa}_\ell$. We choose a moiré Brillouin zone (MBZ) in which the $\boldsymbol{\kappa}_\ell$ is located at the corners, and refer to the MBZ center below as the γ point. The sublattice-dependent interlayer tunneling terms vary periodically with the real space position $\boldsymbol{r}$:

$$T(\boldsymbol{r}) = w\Big[T_0 + e^{-i\boldsymbol{b}_+\cdot\boldsymbol{r}}T_{+1} + e^{-i\boldsymbol{b}_-\cdot\boldsymbol{r}}T_{-1}\Big] \tag{3}$$

where $w \approx 118$ meV [32] and $T_j = \sigma_0 + \cos(2\pi j/3)\sigma_x + \sin(2\pi j/3)\sigma_y$. We use $\boldsymbol{b}$ to denote moiré reciprocal lattice vectors, and $\boldsymbol{b}_\pm = [4\pi/(\sqrt{3}a_M)](\pm 1/2, \sqrt{3}/2)$.

Fig. 1(c) illustrates the $+K$-valley moiré band structure at a rotation angle that is close to the largest magic

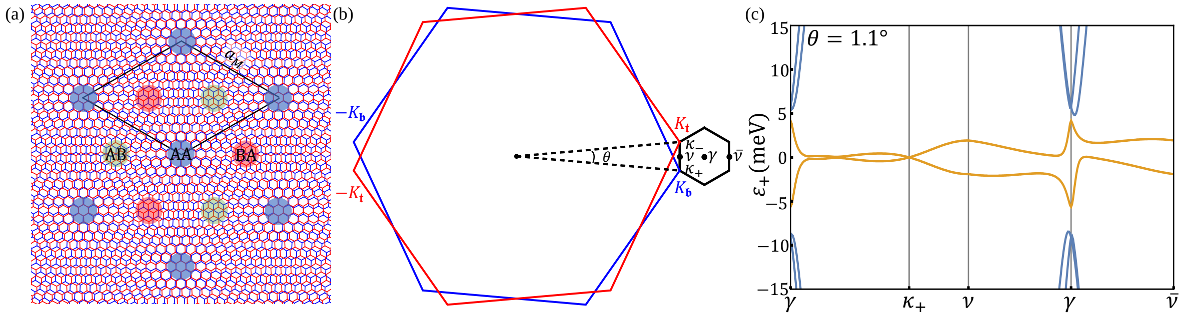

FIG. 1. (a) Real and (b) momentum space structure of twisted bilayer graphene. Low-energy electrons are located in $\pm K$ valleys. (c) moiré bands in $+K$ valley along high-symmetry lines at a twist close to the first magic angle. The spectra along $\nu\gamma$ and $\bar{\nu}\gamma$ lines are different, reflecting the absence of time-reversal symmetry within one valley.

angle. The combined symmetry $\hat{C}_2\hat{\mathcal{T}}$ implies that the Berry curvature of the moiré bands is identically zero, and protects the Dirac cone band touching, and the $\hat{C}_3$ symmetry pins the Dirac cones to the MBZ corners $\boldsymbol{\kappa}_\ell$. Here $\hat{C}_2$ ($\hat{C}_3$) is a twofold (threefold) rotation around $\hat{z}$ axis. The $\hat{\mathcal{M}}_x$ operation maps $\boldsymbol{\kappa}_+$ to $\boldsymbol{\kappa}_-$, and therefore enforces the energy spectra at $\boldsymbol{\kappa}_\pm$ to be identical. The absence of time-reversal symmetry in the single valley Hamiltonian implies that $\varepsilon_\tau(\boldsymbol{q}) \neq \varepsilon_\tau(-\boldsymbol{q})$, where $\tau = \pm$ labels valley and $\boldsymbol{q}$ is momentum relative to the γ point. Microscopic time-reversal invariance instead implies that $\varepsilon_\tau(\boldsymbol{q}) = \varepsilon_{-\tau}(-\boldsymbol{q})$. This feature in the single-particle band structure suggests that intra-valley electron pairing is not energetically favorable. We therefore consider only inter-valley pairing in the following.

The velocity of the Dirac cones at $\boldsymbol{\kappa}_\pm$ varies systematically with twist angle, decreasing from near v_F at large twist angles and crossing through zero at a series of magic twist angles. Near magic angle, the moiré band is nearly flat through much of MBZ, leading to a greatly enhanced density-of-states and opening the way to interaction driven phase transitions. For our choice of parameters, the largest magic angle is 1° if defined by vanishing Dirac velocity, while flat bands with the narrowest bandwidth (∼3 meV) occur at about 1.05°.

Phonon mechanism.— We first study phonon-mediated pairing and then address effects of Coulomb repulsion in the discussion below. We have considered a variety of phonon modes as discussed in the Supplemental Material [33], and found that in-plane optical phonon

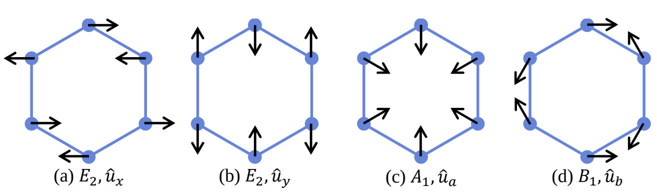

FIG. 2. Illustration of the atomic displacements in the four phonon modes. Each blue dot represents a carbon atom.

modes associated with each graphene layer have a particularly strong effect on the pairing. These modes yield weak phonon-mediated interlayer interactions [34], which we will neglect. With this simplification we can follow the monolayer analysis in Ref. 35 which identifies four in-plane phonon modes that couple strongly to low-energy electrons: (i) the doubly degenerate E_2 modes in the vicinity of the Γ point and (ii) the A_1 and B_1 modes, which are combinations of phonon modes near $\pm K$. The atomic displacements associated with the four modes are illustrated in Fig. 2. The Γ and $\pm K$ point phonon modes lead respectively to intra and inter-valley scattering. The isolated layer electron-phonon coupling Hamiltonian is:

$$\begin{aligned} H_{\rm EPC} = \int d^2\boldsymbol{r}\hat{\psi}^\dagger(\boldsymbol{r})\{&F_{E_2}[\hat{u}_x(\boldsymbol{r})\tau_z\sigma_y - \hat{u}_y(\boldsymbol{r})\sigma_x] \\ &+F_{A_1}[\hat{u}_a(\boldsymbol{r})\tau_x\sigma_x + \hat{u}_b(\boldsymbol{r})\tau_y\sigma_x]\}\hat{\psi}(\boldsymbol{r}), \end{aligned} \tag{4}$$

where $\hat{u}_{x,y}$ and $\hat{u}_{a,b}$ are the normal mode coordinates of the two E_2 modes, and of the A_1 and B_1 modes respectively, $\tau_{x,y,z}$ are Pauli matrices in valley space, and the operator $\hat{\psi}$ is a spinor in sublattice-valley space: $(\hat{\psi}_{+A}, \hat{\psi}_{+B}, \hat{\psi}_{-A}, \hat{\psi}_{-B})^{\rm T}$. (The subscripts $\pm$ refer to $\pm K$ valleys, A and B label sublattices, and the layer and spin indices are hidden.) In a nearest-neighbor tight-binding model, the coupling constants $F_{E_2} = F_{A_1} = (3/\sqrt{2})(\partial t_0/\partial a_{CC})$, where t_0 and a_{CC} are respectively the nearest-neighbor hopping parameter and distance. When quantized the $\hat{u}_\alpha$ can be expressed in terms of phonon creation and annihilation operators:

$$\hat{u}_\alpha(\boldsymbol{r}) = \sqrt{\frac{\hbar}{2NM\omega_\alpha}}\sum_{\boldsymbol{q}} e^{i\boldsymbol{q}\cdot\boldsymbol{r}}[a_\alpha(\boldsymbol{q}) + a_\alpha^\dagger(-\boldsymbol{q})], \tag{5}$$

where N is the number of A sites in a monolayer, M is the mass of a single carbon atom and ω_α is the frequency of phonon mode α. We neglect the momentum dependence of ω_α below because only phonons that are close to either Γ or $\pm K$ points are important for low-energy electrons; $\hbar\omega_{E_2}$ and $\hbar\omega_{A_1}$ are respectively 0.196 and 0.17 eV in monolayer graphene [35]. Integrating out the phonon modes and neglecting retardation effects because of the high phonon frequencies, we obtain the following phonon-mediated interaction Hamiltonian:

$$H_{\rm att} = -\int d^2\boldsymbol{r}\{g_{E_2}[(\hat{\psi}^\dagger\tau_z\sigma_y\hat{\psi})^2 + (\hat{\psi}^\dagger\sigma_x\hat{\psi})^2] \\ +g_{A_1}[(\hat{\psi}^\dagger\tau_x\sigma_x\hat{\psi})^2 + (\hat{\psi}^\dagger\tau_y\sigma_x\hat{\psi})^2]\}. \quad (6)$$

Here the operators $\hat{\psi}^\dagger$ and $\hat{\psi}$ are understood to be at the same coarse-grained position $\boldsymbol{r}$, and the attractive interaction strength g_α parameters are given by:

$$g_\alpha = \frac{\mathcal{A}}{N}\Big(\frac{F_\alpha}{\hbar\omega_\alpha}\Big)^2\frac{\hbar^2}{2M}, \quad (7)$$

where $\mathcal{A}$ is the sample area. We estimate g_{E_2} and g_{A_1} to be about 52 and 69 meV$\cdot$nm^2 respectively [33].

To study the Cooper pairing instability, we restrict the interaction in (6) to the Bardeen-Cooper-Schrieffer (BCS) channel that pairs electrons from opposite valleys:

$$H_{\rm BCS} = -4\int d^2\boldsymbol{r}\{g_{E_2}[\hat{\psi}^\dagger_{+As}\hat{\psi}^\dagger_{-As'}\hat{\psi}_{-Bs'}\hat{\psi}_{+Bs} + h.c.] \\ +g_{A_1}[\hat{\psi}^\dagger_{+As}\hat{\psi}^\dagger_{-As'}\hat{\psi}_{+Bs'}\hat{\psi}_{-Bs} + h.c.] \\ +g_{A_1}[\hat{\psi}^\dagger_{+As}\hat{\psi}^\dagger_{-Bs'}\hat{\psi}_{+As'}\hat{\psi}_{-Bs} + (A\leftrightarrow B)]\}, \quad (8)$$

where s and s' are spin indices. In $H_{\rm BCS}$, there are two distinct spin-singlet pairing channels: (i) intra-sublattice pairing, e.g., $\epsilon_{ss'}\hat{\psi}^\dagger_{+As}\hat{\psi}^\dagger_{-As'}$ and (ii) inter-sublattice pairing, e.g., $\epsilon_{ss'}\hat{\psi}^\dagger_{+As}\hat{\psi}^\dagger_{-Bs'}$, where ϵ is the fully antisymmetric tensor with $\epsilon_{\uparrow\downarrow}=1$. Only the $\pm K$ phonons contribute to inter-sublattice pairing, which has d-wave symmetry because electrons at different sublattices and opposite valleys share the *same* angular momentum under the threefold rotation $\hat{C}_3\hat{\psi}^\dagger(\boldsymbol{r})\hat{C}_3^{-1} = \exp[i2\pi\sigma_z\tau_z/3]\hat{\psi}^\dagger(\mathcal{R}_3\boldsymbol{r})$. Inter-sublattice Cooper pairs therefore carry a finite angular momentum.

s-wave pairing.— In the s–wave intra-sublattice channel the local pairing amplitude,

$$\Delta^{(s)}_\ell(\boldsymbol{r}) = \langle\hat{\psi}_{-\sigma\ell\downarrow}(\boldsymbol{r})\hat{\psi}_{+\sigma\ell\uparrow}(\boldsymbol{r})\rangle = -\langle\hat{\psi}_{-\sigma\ell\uparrow}(\boldsymbol{r})\hat{\psi}_{+\sigma\ell\downarrow}(\boldsymbol{r})\rangle, \quad (9)$$

is sublattice (σ) independent by symmetry, but we allow a layer (ℓ) dependence. We solve the linearized gap equation by assuming that the pair amplitude has the moiré periodicity and can therefore be expanded in the form $\Delta^{(s)}_\ell(\boldsymbol{r}) = \sum_{\boldsymbol{b}} e^{i\boldsymbol{b}\cdot\boldsymbol{r}}\Delta^{(s)}_{\boldsymbol{b},\ell}$. It follows that

$$\Delta^{(s)}_{\boldsymbol{b},\ell} = \sum_{\boldsymbol{b}'\ell'}\chi^{\ell\ell'}_{\boldsymbol{b}\boldsymbol{b}'}\Delta^{(s)}_{\boldsymbol{b}',\ell'}, \\ \chi^{\ell\ell'}_{\boldsymbol{b}\boldsymbol{b}'} = \frac{2g_0}{\mathcal{A}}\sum_{\boldsymbol{q},n_1,n_2}\Big\{\frac{1-n_F[\varepsilon_{n_1}(\boldsymbol{q})]-n_F[\varepsilon_{n_2}(\boldsymbol{q})]}{\varepsilon_{n_1}(\boldsymbol{q})+\varepsilon_{n_2}(\boldsymbol{q})-2\mu} \\ \times[\langle u_{n_1}(\boldsymbol{q})|u_{n_2}(\boldsymbol{q})\rangle_{\boldsymbol{b},\ell}]^*\langle u_{n_1}(\boldsymbol{q})|u_{n_2}(\boldsymbol{q})\rangle_{\boldsymbol{b}',\ell'}\Big\}, \quad (10)$$

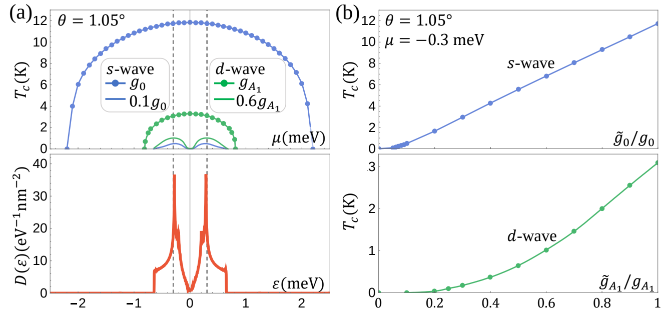

FIG. 3. (a) Critical temperature T_c in s-wave (blue lines) and d-wave channels (green lines) as a function of chemical potential (upper panel), and the DOS per spin and per valley as a function of energy (lower panel) for the twist angle 1.05°. The vertical dashed lines indicate the chemical potential at which the upper or lower flat band is half filled. (b) T_c in s-wave (upper panel) and d-wave (lower panels) channels as a function of reduced attractive interaction strength for $\theta = 1.05°$ and $\mu = -0.3$ meV (half-filling of the lower flat band).

where χ is the pair susceptibility, $g_0 = g_{E_2} + g_{A_1}$, $\boldsymbol{q}$ is a momentum within MBZ, $n_{1,2}$ are moiré band labels in $+K$ valley, ε_n and $|u_n\rangle$ are the corresponding energies and wave functions, $n_F(\varepsilon)$ is the Fermi-Dirac occupation function, and μ is the chemical potential. The overlap function $\langle ...\rangle_{\boldsymbol{b},\ell}$ is the layer-resolved matrix element of the plane-wave operator $\exp(i\boldsymbol{b}\cdot\boldsymbol{r})$. Note that $\hat{\mathcal{T}}$ symmetry has been employed to simplify (10).

The critical temperature T_c is reached when the largest eigenvalue of χ is equal to 1. In Fig. 3(a) we illustrate T_c calculated in this way for $\theta = 1.05°$, including momenta $\boldsymbol{b}$ up to the third moiré reciprocal lattice vector shell. The relatively large T_c values, which exceed 10 K near the magic angle, can be understood by examining the uniform susceptibility, which has the standard $g_0\int d\varepsilon D(\varepsilon)[1-2n_F(\varepsilon)]/[2(\varepsilon-\mu)]$ form, where $D(\varepsilon)$ is the density of states (DOS) per spin and per valley. Because the DOS can reach values of order 10 eV^{-1} nm^{-2}, as illustrated in Fig. 3, the coupling constant $g_0D(\mu)$ can be of order one, corresponding to strong coupling superconductivity. Since the higher-energy bands have much smaller DOS, we have retained only the two flat bands in evaluating (10). The eigenvector of χ with the largest eigenvalue specifies the spatial and layer dependence of the pair amplitude. For s-wave pairing, the pair amplitude is layer independent and concentrated near AA regions in the moiré pattern, as illustrated Fig. 4(a). The spatial variation of $\Delta^{(s)}$ follows the electron density distribution in the normal state of the flat bands. $\Delta^{(s)}$ transforms trivially under all the point-group symmetries, confirming that intra-sublattice pairing is s-wave.

d-wave pairing.— In the inter-sublattice channel, the pair amplitudes $\epsilon_{ss'}\hat{\psi}^\dagger_{+As}\hat{\psi}^\dagger_{-Bs'}$ and $\epsilon_{ss'}\hat{\psi}^\dagger_{+Bs}\hat{\psi}^\dagger_{-As'}$ carry opposite angular momenta corresponding to *chiral* d-wave pairing channels which we refer to as d_+ and d_-

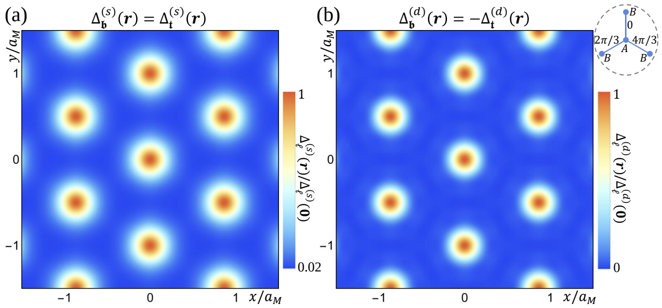

FIG. 4. Real-space map of pair amplitudes $\Delta(\boldsymbol{r})$ that satisfy (a) s-wave and (b) d-wave linearized gap equations for $\theta = 1.05^\circ$ and $\mu = -0.3$ meV. $\Delta(\boldsymbol{r})$ is peaked in the AA regions in both cases. The inset in (b) illustrates d_+ pairing at the atomic scale, where electrons in the same layer but on different sublattices are paired with the indicated bond-dependent phase factors.

respectively. At the atomic scale, chiral d-wave pairing is realized by forming nearest-neighbor spin-singlet Cooper pairs with bond-dependent phase factors, as illustrated in Fig. 4(b). Because of $\hat{\mathcal{T}}$ symmetry, both channels have the same T_c and we therefore focus on d_+ pairing, which has the same susceptibility as in Eq. (10) except that (i) g_0 is replaced by $2g_{A_1}$ and (ii) the overlap functions are replaced by $\langle u_{n_1}(\boldsymbol{q})|\sigma_+|u_{n_2}(\boldsymbol{q})\rangle_{\mathfrak{b},\ell}$, where $\sigma_+ = (\sigma_x + i\sigma_y)/2$. The operator σ_+ is closely related to the velocity operator $\hat{v}_x + i\hat{v}_y$, where $\hbar\hat{\boldsymbol{v}} = \partial\mathcal{H}_+/\partial\boldsymbol{k}$. Near the magic angle, the velocity of the flat bands is strongly suppressed, but the layer counter-flow velocity remains large [12]. As a result, we find that the leading d-wave instability has pair amplitudes of opposite signs in the two layers: $\Delta_{\mathfrak{b}}^{(d)}(\boldsymbol{r}) = -\Delta_{\mathfrak{t}}^{(d)}(\boldsymbol{r})$, where $\Delta_\ell^{(d)} = \langle\hat{\psi}_{-B\ell\downarrow}\hat{\psi}_{+A\ell\uparrow}\rangle$. The highest T_c in d-wave channel at $\theta = 1.05^\circ$ is about 3 K, as shown in Fig. 3(a). The spatial variation of the pair amplitude, illustrated in Fig. 4(b), is similar to the s-wave case. We note that $\Delta_\ell^{(d)}(\boldsymbol{r})$ describes the center-of-mass motion of the Cooper pairs, while the relative motion of the two paired electrons has d-wave symmetry.

Discussion.— Experimentally, magic angle twisted bilayer graphene exhibits superconducting states when the lower energy flat band is near half filled, but not at neutrality ($\mu = 0$) or when the upper flat band is partially occupied [11]. The highest experimental T_c is ~ 1.7 K. It is not yet clear whether or not this stark particle-hole asymmetry, which is absent in our results, is intrinsic or due to an extrinsic disorder effect. We note that the moiré band structure does have intrinsic particle-hole asymmetry as evident in Fig. 1(c), and the asymmetry can be sensitive to the exact model parameters. Even discounting the particle-hole asymmetry, differences remain between experimental and theoretical $T_c(\mu)$ trends in Fig. 3, particularly in connection with the experimental absence of superconductivity at neutrality. Adding a Coulomb contribution to electron-electron interactions weakens the attractive interaction and makes the T_c calculation more like the standard weak-coupling case in which only $g_0 D(\mu)$ is relevant, and could explain the absence of superconductivity at neutrality where $D(\mu)$ has a minimum and often vanishes, as shown in Fig. 3(a).

We account for the Coulomb repulsion using a phenomenological model with only the atomic-scale on-site (U_0) and nearest-neighbor (U_1) repulsion on the honeycomb lattice of each graphene layer. U_0 and U_1 respectively suppress s and d wave pairings [33], and the corresponding attractive interaction strengths in the gap equation are reduced to $\tilde{g}_0 = g_0 - U_0\mathcal{A}_0/2$ and $\tilde{g}_{A_1} = g_{A_1} - 3U_1\mathcal{A}_0/4$, where $\mathcal{A}_0 = \sqrt{3}a_0^2/2$. We have calculated T_c as a function of $\tilde{g}_0$ and $\tilde{g}_{A_1}$ respectively for the two channels [Fig. 3(b)]. If T_c in s-wave channel is fit to the experimental value 1.7 K for a half-filled lower flat band at $\theta = 1.05^\circ$, then U_0 is about 3.7 eV. Similarly, U_1 is about 0.5 eV if d-wave has $T_c \sim 1.7$ K. Depending on the exact values of $U_{0,1}$, either channel can be the leading superconductivity instability. We note that the on-site repulsion U_0 can drive correlated insulating states for integer number of electrons or holes per moiré cell, which has been studied for the charge neutral case [36]. Experimentally, the interaction-induced insulating states at half filling of the lower or upper flat band have a tiny gap of about 0.3 meV [10, 11]. This tiny gap is a possible indication that the Coulomb repulsion is strongly screened, which can be due to the enhanced DOS in the moiré bands, the dielectric encapsulation (hexagonal boron nitride) and the nearby metallic gate that is only 10∼30 nm away from the twisted bilayer [10, 11]. The screening effects require further study, while the phonon-mediated attraction combined with the local repulsion can provide a minimal model to study the competition between the superconducting and the correlated insulating states. Our theory should be taken as a step toward a full quantitative theory of twisted bilayer graphene.

If d-wave is the leading instability, the $d_\pm$ pair amplitudes have identical T_c, and the corresponding superconducting state then has a two-component order parameter that can lead to either chiral or nematic superconductivity. The chiral state is more favored in mean-field theory because it is fully gapped, whereas nematic pairing with spontaneous rotational symmetry breaking results in point nodes. In a follow-up work, we will report that the chiral d-wave state is topological and carries spontaneous bulk supercurrent.

The s and d wave pairings with distinct in-plane phase structures can be distinguished by phase-sensitive experiments [37]. In addition, a peculiar feature of the proposed d-wave superconductivity is that the order parameter has opposite signs on the top and bottom graphene layers, which could also be tested by phase-sensitive measurement. The chiral d-wave state spontaneously breaks time reversal symmetry, which can be examined by Kerr effect and magnetization measurement. Moreover, application of uniaxial strain, which tunes the competition between nematic and chiral d-wave states, in conjunction with upper critical field or critical current measurements could be used to differentiate s and d wave pairings.

Our theory sets up a general framework to study superconductivity in twisted bilayer graphene, and can be used to predict the response of superconductivity to various perturbations, such as electric displacement field, magnetic field, pressure and disorder, which can be compared with coming experimental results.

Acknowledgment.— We thank M. Norman for valuable discussions. Work at Argonne was supported by the Department of Energy, Office of Science, Materials Science and Engineering Division. F. W. was also supported by Laboratory for Physical Sciences. A. H. M. was supported by the Department of Energy, Office of Basic Energy Sciences under grant DE-FG02-02ER45958 and by the Welch foundation under grant TBF1473.

Note added. A new experimental work has recently been posted [38], which demonstrates the tunability of the superconductivity by pressure and also reports the appearance of superconductivity in partially filled upper flat band.

[1] J. M. B. Lopes dos Santos, N. M. R. Peres, and A. H. Castro Neto, Phys. Rev. Lett. **99**, 256802 (2007).
[2] B. Hunt, J. D. Sanchez-Yamagishi, A. F. Young, M. Yankowitz, B. J. LeRoy, K. Watanabe, T. Taniguchi, P. Moon, M. Koshino, P. Jarillo-Herrero, and R. C. Ashoori, Science **340**, 1427 (2013).
[3] C. R. Dean, L. Wang, P. Maher, C. Forsythe, F. Ghahari, Y. Gao, J. Katoch, M. Ishigami, P. Moon, M. Koshino, T. Taniguchi, K. Watanabe, K. L. Shepard, J. Hone, and P. Kim, Nature **497**, 598 (2013).
[4] L. Wang, Y. Gao, B. Wen, Z. Han, T. Taniguchi, K. Watanabe, M. Koshino, J. Hone, and C. R. Dean, Science **350**, 1231 (2015).
[5] K. Kim, A. DaSilva, S. Huang, B. Fallahazad, S. Larentis, T. Taniguchi, K. Watanabe, B. J. LeRoy, A. H. MacDonald, and E. Tutuc, Proc. Natl. Acad. Sci. U.S.A. **114**, 3364 (2017).
[6] G. Chen, L. Jiang, S. Wu, B. Lv, H. Li, K. Watanabe, T. Taniguchi, Z. Shi, Y. Zhang, and F. Wang, arXiv:1803.01985 (2018).
[7] F. Wu, T. Lovorn, and A. H. MacDonald, Phys. Rev. Lett. **118**, 147401 (2017).
[8] F. Wu, T. Lovorn, and A. H. MacDonald, Phys. Rev. B **97**, 035306 (2018).
[9] H. Yu, G.-B. Liu, J. Tang, X. Xu, and W. Yao, Sci. Adv. **3**, e1701696 (2017).
[10] Y. Cao, V. Fatemi, A. Demir, S. Fang, S. L. Tomarken, J. Y. Luo, J. D. Sanchez-Yamagishi, K. Watanabe, T. Taniguchi, E. Kaxiras, R. C. Ashoori, and P. Jarillo-Herrero, Nature **556**, 80 (2018).
[11] Y. Cao, V. Fatemi, S. Fang, K. Watanabe, T. Taniguchi, E. Kaxiras, and P. Jarillo-Herrero, Nature **556**, 43 (2018).
[12] R. Bistritzer and A. H. MacDonald, Proc. Natl. Acad. Sci. U.S.A. **108**, 12233 (2011).
[13] E. Suárez Morell, J. D. Correa, P. Vargas, M. Pacheco, and Z. Barticevic, Phys. Rev. B **82**, 121407 (2010).
[14] G. Trambly de Laissardière, D. Mayou, and L. Magaud, Phys. Rev. B **86**, 125413 (2012).
[15] S. Fang and E. Kaxiras, Phys. Rev. B **93**, 235153 (2016).
[16] C. Xu and L. Balents, Phys. Rev. Lett. **121**, 087001 (2018).
[17] N. F. Q. Yuan and L. Fu, Phys. Rev. B **98**, 045103 (2018).
[18] H. C. Po, L. Zou, A. Vishwanath, and T. Senthil, Phys. Rev. X **8**, 031089 (2018).
[19] G. Baskaran, arXiv:1804.00627 (2018).
[20] B. Padhi, C. Setty, and P. W. Phillips, Nano Lett. **18**, 6175 (2018).
[21] J. F. Dodaro, S. A. Kivelson, Y. Schattner, X. Q. Sun, and C. Wang, Phys. Rev. B **98**, 075154 (2018).
[22] C.-C. Liu, L.-D. Zhang, W.-Q. Chen, and F. Yang, arXiv:1804.10009 (2018).
[23] T. J. Peltonen, R. Ojajärvi, and T. T. Heikkilä, arXiv:1805.01039 (2018).
[24] J. Kang and O. Vafek, Phys. Rev. X **8**, 031088 (2018).
[25] L. Rademaker and P. Mellado, arXiv:1805.05294 (2018).
[26] D. M. Kennes, J. Lischner, and C. Karrasch, arXiv:1805.06310 (2018).
[27] H. Isobe, N. F. Q. Yuan, and L. Fu, arXiv:1805.06449 (2018).
[28] M. Koshino, N. F. Q. Yuan, T. Koretsune, M. Ochi, K. Kuroki, and L. Fu, Phys. Rev. X **8**, 031087 (2018).
[29] Y.-Z. You and A. Vishwanath, arXiv:1805.06867 (2018).
[30] D. Huertas-Hernando, F. Guinea, and A. Brataas, Phys. Rev. B **74**, 155426 (2006).
[31] H. Min, J. E. Hill, N. A. Sinitsyn, B. R. Sahu, L. Kleinman, and A. H. MacDonald, Phys. Rev. B **74**, 165310 (2006).
[32] J. Jung, A. Raoux, Z. Qiao, and A. H. MacDonald, Phys. Rev. B **89**, 205414 (2014).
[33] See Supplemental Material at URL for additional discussion on the electron-phonon coupling, the Coulomb repulsion effects, the twist angle dependence of the critical temperature and the coherence length, which includes Refs. [39–41].
[34] J.-A. Yan, W. Y. Ruan, and M. Y. Chou, Phys. Rev. B **77**, 125401 (2008).
[35] D. M. Basko and I. L. Aleiner, Phys. Rev. B **77**, 041409 (2008).
[36] L. A. Gonzalez-Arraga, J. L. Lado, F. Guinea, and P. San-Jose, Phys. Rev. Lett. **119**, 107201 (2017).
[37] D. J. Van Harlingen, Rev. Mod. Phys. **67**, 515 (1995).
[38] M. Yankowitz, S. Chen, H. Polshyn, K. Watanabe, T. Taniguchi, D. Graf, A. F. Young, and C. R. Dean, arXiv:1808.07865 (2018).
[39] R. M. Ribeiro, V. M. Pereira, N. M. R. Peres, P. R. Briddon, and A. H. C. Neto, New Journal of Physics **11**, 115002 (2009).
[40] B. Roy, J. D. Sau, and S. Das Sarma, Phys. Rev. B **89**, 165119 (2014).
[41] T. O. Wehling, E. Şaşıoğlu, C. Friedrich, A. I. Lichtenstein, M. I. Katsnelson, and S. Blügel, Phys. Rev. Lett. **106**, 236805 (2011).